Identification of interlaminar fracture properties of a composite laminate using local full-field kinematic measurements and finite element simulations

Florent Mathieu, Patrick Aimedieu, Jean-Mathieu Guimard, François Hild

Identification of interlaminar fracture properties of a composite laminate using local full-field kinematic measurements and finite element simulations

Florent Mathieu[a], Patrick Aimedieu[a], Jean-Mathieu Guimard[b], François Hild[a,*]

[a] *Laboratoire de Mécanique et Technologie (LMT-Cachan)*
ENS Cachan / CNRS / UPMC / PRES UniverSud Paris
61 Avenue du Président Wilson, F-94235 Cachan Cedex, France
[b] *EADS France - Innovation Works, 12 rue Pasteur, F-92152 Suresnes, France*

Abstract

The paper is devoted to the identification of interlaminar properties by analyzing three tests with different mode mixities on a unidirectional thermoset composite material. It is shown that by coupling digital image correlation with finite element simulations, it is possible to locally extract energy release rates whose standard uncertainty is at most equal to 50 J/m^2. This performance is achieved with a standard finite element code by optimizing the location of the crack tip, which is the key information needed to evaluate (linear elastic) fracture mechanics parameters of these materials. The level of stress intensity factors and the experimental mode mixity can be identified in all configurations with an acceptable uncertainty.

Keywords: A. Carbon Fiber Reinforced Plastics (CFRPs); B. Delamination; C. Finite element analysis (FEA); D. Mechanical testing.

*Corresponding author. Phone: +33 1 47 40 21 92, Fax: +33 1 47 40 22 40.
Email addresses: florent.mathieu@lmt.ens-cachan.fr (Florent Mathieu), patrick.aimedieu@lmt.ens-cachan.fr (Patrick Aimedieu), jean-mathieu.guimard@eads.net (Jean-Mathieu Guimard), francois.hild@lmt.ens-cachan.fr (François Hild)

1. Introduction

The general context of this study is related to the intensive use of composite materials in aerospace structures. Besides the known and interesting mechanical properties of these materials, it is important to know their cracking properties with a high confidence to design structures up to failure. The modeling capabilities, for instance at the mesoscale (*i.e.,* at the ply level [1]), are currently used [2]. These types of models need for each material (and more precisely for the ply and interface entities to be modeled) to perform an identification process at the coupon scale. The identification procedure proposed herein is only devoted to the interface cracking parameters of a unidirectional thermoset composite material T700/M21 (from pre-preg cured with industrial quality process). More precisely, it consists in performing fracture mechanics based tests in dominant modes with a pre-crack. The geometries chosen in the present case are the double cantilever beam (DCB) test [3] for the mode I, and the CLS (*i.e.,* crack lap shear) test [4] for mode II or mixed mode characterization. Such tests enable the critical energy release rates, which are directly connected to the intrinsic parameters of interface models [5], to be extracted. The aim of the present paper is to propose a new extraction method with an acceptable accuracy with respect to reference methods, which can give confidence when applied to more complex delamination tests. Furthermore, it allows to determine quantities that are very difficult to assess experimentally such as the actual mode mixity, which is directly related to the actual boundary conditions. Last, the detection of propagation onset is also possible.

When identifying models for adhesive or cohesive layers, *point* data, *e.g.,* displacement, strain and load, usually are the only experimental information available [6], see an example of force vs. displacement curve for a DCB test in Figure 1. The expected $\mathcal{G}_c$ values of the critical energy release rate are then

computed from any classical beam assumptions, through the definition of the energy release rate $\mathcal{G}$ [7]. Pictures shot at different scales are also used in a qualitative way in addition to global data [8, 9, 10, 11], or quantitatively by evaluating deflections [12, 13], deformed shapes [14], and more detailed displacement fields [15, 16]. In this study, it is proposed to use quantitatively full-field measurements provided by Digital Image Correlation (DIC) to determine displacement fields in DCB and CLS experiments for identification purposes. These two experimental configurations are classical when evaluating interlaminar properties of composite materials [17]. The advantage of DIC lies in the fact that displacement *fields* are available to analyze an experiment, as opposed to standard procedures using few data [3, 18, 19, 4]. These displacement fields typically contain 1,000 to 10,000 degrees of freedom. In particular, it is possible to know the experimental boundary conditions. Furthermore, the 2D local displacement field near the crack tip is accessible at the right scale and with a good accuracy during propagation, so that other intrinsic interface parameters may be identified without taking into account any global displacement and load values, provided the elastic properties of the plies are known. The measured displacements can be used to determine interlaminar parameters for each recorded image during loading, contrary to IGC [18] or AITM [19] methods that respectively extract one propagation value per cycle of small propagation path or only a single value for the whole propagation regime of the test (Figure 1). As mentioned above, the present analysis also includes a quantitative evaluation of the mode mixity during the experiment, an information that is not provided by IGC or AITM methods but only from theoretical pre-test assumptions.

Figure 1 about here

DIC has seen many developments during the last decade [20] for several reasons. First, it is generally simple and easy to apply under natural light.

Its resolution is now sufficient to analyze experiments performed at various scales [21, 22, 23, 24]. DIC is usually based upon local registration of interrogation windows in a series of pictures. In the present case, a finite-element discretization of the displacement field [25] will be used to prescribe the loading conditions on the external part of the region of interest. This approach allows us to couple *seamlessly* measurements and computations to extract fracture mechanics parameters. There are many studies that have attempted to enrich experimental databases by resorting to full-field measurements [26, 27, 15, 28, 29, 30]. However, the identification of fracture parameters and cohesive models remains an experimental challenge because displacements need to be measured at very fine scales [31, 16]. For instance, Abanto-Bueno and Lambros [31] used a multi-camera system to determine the traction separation law of a photodegradable copolymer. In the present work, only a local analysis with a single camera is performed to evaluate linear elastic fracture mechanics parameters via a coupling with finite element simulations. Among those parameters, the crack tip location is key information from which all the others are subsequently obtained.

The inverse procedure is applied to the characterization of delamination properties of a 0 / 0° interface configuration of a carbon-epoxy composite in DCB and CLS tests (Section 2). A series of pictures is analyzed by a finite element based DIC algorithm [25] during crack opening, and subsequent propagation steps. Energy release rates and stress intensity factors are evaluated in both cases by using the commercial code Abaqus [32] and user-developed Matlab scripts. The internal points of the mesh are used to determine the crack tip location by minimizing the distance between measured and computed displacements (Section 3). In Section 4, all the previous tests are finally analyzed and discussed. The changes of crack tip location, stress intensity factors, energy release rates, and mode mixities with the applied load are reported.

2. Experimental set-up and protocol for the two configurations

In the sequel, three experimental configurations are analyzed. The DCB experiment allows for the identification of mode I properties as the crack is mainly loaded under mode I condition [3]. In that case, the zone around the crack tip can be observed when the crack was opening and subsequently propagating. The two CLS configurations studied herein lead to predominantly mode II cracking [4]. First, the analysis is performed with no apparent crack propagation, and second, with crack propagation. The experiments are monitored by a Canon EOS 350D camera with a Sigma lens, focal length: 180 mm.

2.1. DCB configuration

A DCB sample is first analyzed. Its geometry is shown in Figure 2(a). The corresponding dimensions are $b = 20$ mm, $h_1 = 2.15$ mm, $h_2 = 1.85$ mm, $L = 250$ mm, and $t = 20$ mm. All the plies are aligned along the 0°-degree direction (or y-axis, see Figure 2(a)) perpendicular to the loading direction (*i.e.,* x-axis), and there is a pre-crack of length a_0 at the separation plane. The sample was loaded under a displacement controlled procedure. In the following, the end of the loading step will be analyzed.

Figure 2 about here

Figure 2 shows three pictures of the experiment, namely, the reference one and two of the surface in its deformed configuration. They are used to measure displacements via Q4-DIC [25] in which the displacement field is based upon a finite element discretization with 4-noded bilinear (Q4) elements. The commercial code Correli$^{\mathrm{STC}}$® was used [33]. In the present case, the size of each element edge is equal to 16 pixels (or ≈ 200 μm). The corresponding transverse displacement fields are shown. The presence of the crack is clearly seen on both pictures and on the displacement fields themselves.

2.2. CLS configurations

The modified Cracked Lap Shear (CLS) or mode II test configuration is shown in Figure 3(a). It consists in a tensile-like specimen made of plies aligned along the 0°-direction with respect to the loading direction. The dimensions are $b = 10$ mm, $h_1 = 1.6$ mm, $h_2 = 1.9$ mm, $L = 350$ mm with a pre-crack of length a_0 at the separation plane. In such conditions, a longitudinal displacement applied on one arm in conjunction with a clamped condition at the other end of the specimen leads to a mixed crack propagation mode. Two lateral confinements (in the x-direction, see Figure 3(a)) are put into contact with the external surfaces in order to avoid opening and as a consequence prevent any mode I contributions (as will be shown hereafter, the loads introduced by the grips are of second order of magnitude with respect to the longitudinal loads).

Figure 3 about here

This geometry has several advantages. First, it enables for the use of the same device for static and dynamic tests to ensure that comparisons are made on the same basis in a quasi pure mode II. Second, the propagation is confined to a longitudinal domain. The determination of the loading possibly transmitted to the specimen does not involve any complex analysis. A first order estimate of the critical value $\mathcal{G}_c$ of the energy release rate is determined by using a classical beam solution for a steady state value [4]

$$\mathcal{G}_c = \frac{F_c^2 h_2}{2E_1 b^2 h_1 (h_1 + h_2)} \tag{1}$$

where F_c is the maximum load level, b the width of the sample, and E_1 the Young's modulus in the longitudinal direction.

A first propagation is sought in a displacement controlled manner. The main difficulty of this type of experiment is then related to the location of the crack

tip. This task is performed by resorting to Q4-DIC [25]. The size of each element edge is equal to 32 pixels (or ≈ 200 μm) ; it is chosen since it corresponds to a good compromise between uncertainty level and spatial resolution. As soon as the first propagation occurs, the sample is unloaded, and then subsequently loaded up to a level of 5 kN. The crack is maintained open and the camera is moved until the crack tip is located at about the center of the picture. Figure 3(b) shows a displacement field in which the presence of a crack is clearly distinguished. The exact position of the crack tip is still unknown. It will be determined more precisely in the sequel.

After the crack is detected in the picture, four additional pictures are shot every 1 kN. For a load level of 9.6 kN, unstable (or undetermined) crack propagation occurred. No additional pictures are taken. The CLS configuration is theoretically quasi-unstable since the first derivative of $\mathcal{G}$ with respect to the crack length is equal to 0 (see Equation (1)). The analysis of this experiment consists of the five displacement fields corresponding to load levels ranging from 5 to 9 kN.

In the second experiment, no lateral confinement (*i.e.,* no grips) is applied and the mode mixity is induced by the experimental configuration itself. The dimensions of the sample are $b = 10$ mm, $h_1 = 1.61$ mm, $h_2 = 1.57$ mm, and $L = 250$ mm. Two different steps are analyzed. First, the initiation of propagation of the pre-crack close to the groove of the CLS sample is studied. Thirteen loading steps are analyzed. The subsequent propagation was not monitored, but the crack did not cross the whole sample. The next task is then to determine a rough estimate of the crack tip position so that the camera can be moved. The sample is then reloaded (20 loading steps are available) and the beginning of the new propagation step is followed (with 11 pictures). One key issue of this experiment is related to the actual mode mixity and its change during the various loading steps.

3. Identification procedure of fracture mechanics parameters

The following analyses are based upon measured displacement fields $\mathbf{u}_{meas}$ by resorting to Q4-DIC (*e.g.,* Figures 2 and 3). This is the only experimental information that will be used herein. By prescribing the displacements of the external boundary of the region of interest (ROI, see Figure 4(a)) to a finite element calculation of the *same* part (Figure 4(b)), the way the external load is applied to the crack is accounted for. There is therefore no need to model the whole experiment, but only the part inside the ROI [16]. The computed displacements $\mathbf{u}_{comp}$ of all inner nodes are used to determine the crack tip position $\mathbf{x}_c$, the first unknown of the fracture mechanics problem. In the present study, a simple definition of the crack tip location is considered. It corresponds to the location for which the identification error between the measured and computed displacement field is the smallest. It can be noted that other approaches might have been considered (*e.g.,* damage mechanics, cohesive zone model) for which the existence of a crack tip is not necessarily needed. The identification error

$$\delta^2(\mathbf{x}_c) = \frac{1}{n_m} \sum_{m=1}^{n_m} \|\mathbf{u}_{meas}(\mathbf{x}_m) - \mathbf{u}_{comp}(\mathbf{x}_m, \mathbf{x}_c)\|^2 \tag{2}$$

is minimized with respect to $\mathbf{x}_c$, where n_m is the number of measurement nodes located at $\mathbf{x}_m$. Various crack positions are considered along the crack surface direction. Each node of the interface is scanned to define a crack tip (Figure 4(b)), and the best position corresponds to the minimum value of the displacement residual δ (Figure 4(c); it corresponds to the 56-th node number in that case).

Figure 4 about here

In the finite element analyses reported hereafter, the behavior of the composite is assumed to be elastic. The elastic properties of the two 0-degree laminates are as follows, $E_1 = 120$ GPa, $G_{12} = 5.3$ GPa, $E_2 = E_{33} = 8.9$ GPa, $\nu_{13} = \nu_{12} = 0.33$, $\nu_{23} = 0.35$, where the longitudinal direction of the ply is 1, the

transverse direction is 2, and the out-of-plane one 3. These values were determined in another identification process by performing a series of tensile tests on [0°], [± 45°], [± 67.5°] configurations with loading and unloading sequences [1].

The mesh used in the simulations is refined in comparison with the measurement discretization to achieve a finer resolution for the detection of the crack tip. All the points of Q4-DIC are part of the simulation. Consequently, the differences are still performed on the *common* nodes of the two meshes so that the error is evaluated with respect to the same number of nodes, irrespective of the discretization used. A refinement index ρ is defined such that the number of numerical elements is equal to ρ^2 times that of the measurement elements. The sensitivity of the identification results to the discretization will be studied hereafter. It is worth noting that this refinement is possible thanks to the Q4 interpolation so that no interpolation error on the correlation results is added.

The crack tip position being found (Figure 4(d)), the computed displacement field is post-processed by using fracture mechanics tools available in the finite element code. In the present case, the energy release rate $\mathcal{G}$ and the stress intensity factors (SIFs) are evaluated in orthotropic media [34] by using contour integrals [35]. A sensitivity analysis to the size of the integration domain is performed to check that the results have reached a value that becomes domain-independent as expected from a J-integral [36] or an interaction integral [37]. Figure 5 shows the change of $\mathcal{G}$ with the external radius of the integration domain. When the radius is greater than 32 pixels the evaluation is virtually insensitive to the size of the integration domain, namely, a fluctuation less than 0.5 % is observed. This minimum radius is equal to the element size of the DIC analysis. This result shows that the minimum size of the integration domain is equal to two elements. In all the analyses that will follow, it was checked that $\mathcal{G}$-values are in a region where the results are independent of the size of the integration domain.

Figure 5 about here

4. Analysis of the three different tests

The various (linear elastic) fracture mechanics parameters are extracted by following the previous procedure for the three tests introduced above.

4.1. DCB experiment

The DCB experiment allows for analyses in which propagation is stable under a displacement controlled test. A series of 28 pictures is considered in addition to the reference picture. One of the aims of the present analysis is to determine which pictures correspond to a situation where propagation does not occur. Further, if propagation occurs, is it under constant $\mathcal{G}$-value? Figure 6 shows a comparison between the measured and computed displacement fields for one of the highest load levels of the series. The residual map is also shown to evaluate the quality of the identification. Except in the immediate vicinity of the crack surface, the residuals are very small (*i.e.,* less than 0.5 pixel or 6 μm). This is to be expected since a Q4-DIC analysis is performed without any discontinuous kinematic enrichment.

Figure 6 about here

Figure 7 shows the change of the identification error δ as a function of the applied load for three different discretizations. The identification error is independent of the discretization level when $\rho \geq 2$. The case $\rho = 1$ leads to results different from the reported ones. Two regimes are observed. First, when the crack does not propagate (and the load level increases), the identification error is of the order of 0.2 pixel (or 2.4 μm). This value is larger than the standard displacement uncertainty (of the order of 0.04 pixel or 0.5 μm). It is explained by the fact that a purely elastic model is only a first order approximation of the

interfacial and intralaminar behavior. Second, when the crack propagates (and the load level decreases), there is a gradual increase of the identification error. The last points are likely to be less well tuned. One reason is that the crack tip moves closer to the edge of the region of interest and less measurement points exist in the ligament so that the evaluation of the energy release rate is less accurate.

Figure 7 about here

The location of the crack tip as a function of the load level is shown in Figure 8. Three different refinements are used. The root mean square (RMS) difference between these three results is less than 5 pixels (*i.e.,* 60 μm). A very small effect of the discretization is observed. When analyzing the first 12 points (for which the load level increases), it is seen that the standard uncertainty of the crack tip location is of the order of 14 pixels (or 170 μm). For the last 16 points (for which the load level decreases), there is a clear motion of the crack tip. When a linear interpolation is used, the level of fluctuations is equal to 10 pixels (*i.e.,* 120 μm), which is close to the previous value. It is therefore believed that the local fluctuations are an indication of the identification uncertainty rather than of physical origin. When compared to classical methods where a visual inspection of the crack size is performed (*i.e.,* with a $\pm$ 500 μm resolution), there is a clear benefit of using the approach developed herein, which is mechanically-based.

Figure 8 about here

Figure 9 shows the change of the energy release rate $\mathcal{G}$ with the applied load for the 28 analyzed pictures. The RMS difference between the three refinements is equal to 15 J/m^2. This low value is consistent with the previous results in terms of crack tip location. In terms of overall result, there are two distinct

trends when the first 12 points are considered in comparison with the last 16 ones. This difference is related to the fact that propagation has occurred for the latter ones. In the first part, a parabolic interpolation leads to a RMS error of about 50 J/m^2, as well as with a constant level for the second part (for which $\mathcal{G}_c = 410 \pm 50$ J/m^2).

Figure 9 about here

To analyze further the effect of the crack tip location, the first nine points for which the load variation is less than 5 N are considered. The evaluation of $\mathcal{G}$ performed before is compared with that obtained with a constant crack tip location. Figure 10 shows the correlation obtained when comparing these two ways of identifying $\mathcal{G}$ values. The RMS difference is of the order of 50 J/m^2. These levels of uncertainty are in accordance with those obtained by a classical global method [3] based on load measurements. This level proves that the fluctuations observed in $\mathcal{G}$-values are related to the uncertainty of crack tip position. Therefore it is believed that the fluctuations observed during the propagation stage are essentially related to measurement and identification uncertainties, and not to physical phenomena due to, say, local variations in interfacial properties, which are known to remain small in the present configuration.

Figure 10 about here

Last, the mode mixity is studied during the two steps of cracking. The fact that the two beam thicknesses are slightly different may induce some mixity. The ratio $\mathcal{G}_I/\mathcal{G}_{II}$ reaches high values, on average equal to 17. This value is virtually independent of the refinement index, and therefore assumed to be physical. The mixity remains of the same order of magnitude prior to and during the propagation step, with a negligible part of mode II contribution (*i.e.,* 27 J/m^2 on average). The DCB test is therefore not only mode I dominant, but purely mode I in the present configuration.

4.2. CLS experiments

4.2.1. Modified CLS experiment

In the modified CLS experiment reported herein, propagation is mainly unstable and the analysis is restricted to the 5 load levels for which pictures were shot. An additional information is given by the maximum load F_c that the sample could sustain after the series of pictures was taken ($F_c = 9.6$ kN). With that information, the critical value $\mathcal{G}_c$ is determined by using Equation (1). With the material parameters given above, $\mathcal{G}_c = 1320$ J/m^2. This value will be compared with those obtained by analyzing the 5 load levels with the above-described procedure.

Figure 11 shows a comparison between the measured and computed displacement fields for the 9 kN load level. The residual map is also shown to evaluate the quality of the identification. An identification error of 0.3 pixel (or 1.8 μm) is found. This value is small in terms of physical quantity, however larger than the measurement uncertainty evaluated to be of the order of 0.05 pixel (or 0.3 μm). When analyzing the residual maps (Figure 11(e,f)), the maximum values are for the elements cut by the crack in the measured data. This is to be expected since a Q4-DIC analysis was performed without any discontinuous kinematic enrichment. When this zone is left out for the evaluation of the residuals, the identification error decreases to 0.25 pixel (or 1.5 μm). The same trend is observed for the four analyzed cases.

Figure 11 about here

In the following analysis, the mesh used in the simulations is again refined in comparison with the measurement discretization. Figure 12(a) shows the change of $\mathcal{G}$ with the applied load for different values of ρ. The results are weakly dependent on the discretization when $\rho \geq 2$. The results with $\rho = 1$ are completely different from those reported in Figure 12(a) and are not shown. An

overall standard deviation less than 20 J/m^2 is observed, which is acceptable and in line with classical deviations reached with global identification methods. Figure 12(b) shows the mean values obtained with the five analyzed load levels, and the one obtained from the knowledge of the maximum load level (hexagram). If the results of the five load levels were extrapolated to the maximum load, they would reach a value of the order of 1250-1350 J/m^2, in good agreement with the value found previously (*i.e.,* 1320 J/m^2).

Figure 12 about here

In terms of identification residuals, Figure 13 shows the change of the identification error δ as a function of the applied load. The range of δ varies between 0.15 and 0.25 pixel (or $0.9 - 1.5$ μm). There is a clear degradation when the applied load level increases. The fact that the order of magnitude of the error remains the same indicates that the overall quality of identification does not change. These levels show that even though the agreement between measured and identified fields is good, a purely elastic description of the behavior of the interface and the plies is only a first order approximation of the true one. Last, the influence of the discretization is weak on the overall identification quality when $\rho > 1$. This trend is to be expected by analyzing the results shown in Figure 12(a). The case $\rho = 1$ leads to residuals that are systematically higher than those observed for $\rho \geq 1$. There is therefore a clear benefit in using a more refined FE mesh. However, a very fine mesh is not needed since the results are virtually mesh-independent as soon as $\rho \geq 2$.

Figure 13 about here

The location of the crack tip as a function of the load level is shown in Figure 14. It is worth noting that the crack tip location is directly related to the underlying finite element mesh, namely, each node along the crack path is

considered (Figure 4). For the first three load levels, there is a ± 20 pixel (or ± 120 μm, which is in all cases more accurate than any visual inspection used in classical methods) difference in the location of the crack tip when different meshes are used. Conversely, for the last two load levels, all results are virtually identical for ρ greater than 3. Larger values of ρ allow for a better spatial resolution of the crack tip position. The fact that the crack tip moves as the load level is increased is related to its opening that becomes more easily quantified and identified.

Figure 14 about here

The mode mixity is finally addressed. The point of using lateral confinement was to minimize the mode I contribution. The ratio $\mathcal{G}_I/\mathcal{G}_{II}$ will thus be analyzed for the two CLS configurations studied herein. Figure 15 shows the change of $\mathcal{G}_I/\mathcal{G}_{II}$ with the applied load for the five different mesh densities. Contrary to what is observed for $\mathcal{G}$ and the crack tip position, the ratio $\mathcal{G}_I/\mathcal{G}_{II}$ fluctuates more due to small variations in $\mathcal{G}_I$ (± 20 J/m^2) for levels varying between 20 and 60 J/m^2. For the highest load level, the mean $\mathcal{G}_I/\mathcal{G}_{II}$ ratio is equal to 0.12 for the five discretizations. Even though there are fluctuations with the applied load, the mode mixity remains low during the load history. It is in accordance with a mode II dominant configuration and below the classical value without confinement, *i.e.,* a mean ratio of about 0.20 is classically reported [38, 39]. The difficulty to set up the confinement supports and the local extraction (instead of global one) are explanations to this difference. The main point is that the present method captures all mode mixity effects whatever the condition and configuration of the actual test.

Figure 15 about here

4.2.2. Standard CLS experiment

To compare the mode mixity observed in the previous configuration, a standard CLS experiment is also performed. In all the analyses to follow, a value of the refinement index $\rho = 2$ is chosen. Two different phases are analyzed. The initiation of the first crack, which is always delicate since it depends on the sample preparation and in particular on the details of the bonding state close to the teflon tape. Because propagation may be very quickly unstable, this first step is critical in CLS experiments as shown above. Figure 16 shows the change of $\mathcal{G}$ with the applied load. The dashed line shows that a quadratic interpolation is a very good approximation of the $\mathcal{G}$ vs. applied load curve. The RMS difference between the predicted and measured values is less than 70 J/m^2. This value is close to the estimated uncertainty of $\mathcal{G}$ values (*i.e.,* 50 J/m^2), thereby indicating that a quadratic interpolation is a good estimate of the dependence of $\mathcal{G}$ with the applied load.

Figure 16 about here

With the same material parameters as above, the application of Equation (1) leads to $\mathcal{G}_c = 1260$ J/m^2 for the maximum applied load ($F_c = 9.9$ kN). This value is significantly lower than what is identified with the proposed approach (*i.e.,* $\mathcal{G}_c = 2100$ J/m^2, see Figure 16). It is worth remembering that an initial crack is not necessarily present and therefore the applicability of Equation (1) is not guaranteed (*i.e.,* no steady state propagation is observed). The fact that a very high initiation value is found explains why the observation of subsequent propagation is very difficult in this type of test. Since a lot of elastic energy is stored prior to propagation, it may be sufficient to induce a very significant propagation before the crack stops.

One key information in CLS experiments and for the present identification method is related to the mode mixity. Figure 17 shows the change of the ratio

$\mathcal{G}_I/\mathcal{G}_{II}$ with the applied load. The ratio remains less than 0.08 throughout the whole loading sequence for which no propagation occurs. It is therefore concluded that the initiation stage is mainly mode II controlled. However, the initial loading does not proceed with a constant mode mixity. Close to the maximum load level for which a picture is recorded, the initiation itself is mode II dominant. The fluctuations of mode mixity may explain part of the difference observed in terms of dependence of $\mathcal{G}$ with the applied load. For orthotropic media, a complex coupling appears between $\mathcal{G}_I$ and $\mathcal{G}_{II}$ that does not lead to a linear dependence (classically known for isotropic media) [34].

Figure 17 about here

This is confirmed by analyzing the changes of the two SIFs with the applied load (Figure 18). The mode II SIF follows a linear dependence with the applied load whereas the mode I SIF fluctuates during the whole loading history. These fluctuations, which are very difficult to control experimentally, are responsible for the small variations around a quadratic response of $\mathcal{G}$. Last, when compared with the previous CLS configuration, it is observed that the $\mathcal{G}_I/\mathcal{G}_{II}$ ratio becomes even smaller without any lateral confinement.

Figure 18 about here

Even though a very high value of $\mathcal{G}$ is observed in the initiation stage (Figure 16), the crack does not traverse the whole sample. It stops at about the middle length of the beam. The displacement is then decreased to a very small value. After roughly locating the crack tip by visually analyzing the displacement maps provided by Q4-DIC, the applied displacement is increased again. In the present case, it is possible to follow the beginning of propagation until the crack tip is no longer located in the picture. Figure 19 shows the change of $\mathcal{G}$ with the applied load during the two stages (*i.e.,* no propagation and sub-

sequent propagation). The first stage leads to a quasi quadratic $\mathcal{G}$ vs. applied load trend as previously observed.

Figure 19 about here

The deviation from the quadratic response is again due to the value of mode I SIF that varies significantly during the first loading part. It leads to very high values of mode mixity (Figure 20) especially at the beginning of the loading history. This may be due to loading conditions that are not strictly those associated with a CLS geometry due to small misalignments. It is worth remembering that this type of analysis is only possible when these various quantities are extracted with the true experimental conditions (*i.e.,* the displacements on the boundary of the ROI).

Figure 20 about here

During propagation, there is a clear increase of $\mathcal{G}$ as the load level decreases (see inset of Figure 19). An interpolation by the inverse of the applied load captures the trend observed experimentally. Contrary to the first part of the loading history, this second part is characterized by a slight increase of mode mixity $\mathcal{G}_I/\mathcal{G}_{II}$ from 0.09 to 0.12 (Figure 20). The value at the onset of propagation is below the mean estimate without confinement (*i.e.,* 0.20 [38, 39]) and is below the ratio obtained with confinement. The difficulty to set up the lateral confinements is again pointed out. In spite of this complex preparation, the present local extraction gives good tendencies and more accurate estimates than only from a classical (global) analysis, which does not give access to actual (and varying) mode mixities.

When compared with the modified CLS configuration, the same level of $\mathcal{G}_I/\mathcal{G}_{II}$ ratio is observed. The effect of lateral confinement is therefore minimal at best, and seems useful only at the beginning of loading. There is a clear

deviation from the value as propagation proceeds. This result proves that propagation is not under a constant mode mixity and that the present method is able to capture it. The fact $\mathcal{G}_c$ increases with the crack length may be due to an R-curve behavior since an increase of the mode mixity cannot explain the increase in toughness (since these materials are classically known to have $\mathcal{G}_c$-values that are significantly higher under mode II propagation compared with mode I propagation [40]).

Last, with the material parameters given above, $J_c = 860$ J/m^2 for the maximum applied load ($F_c = 8.3$ kN). This value is of the same order of magnitude, yet lower than what is identified during the propagation stage (*i.e.,* $\mathcal{G}_c = 670 - 730$ J/m^2, see inset of Figure 19). This trend is identical for all the cases studied herein.

4.3. Discussion

In the present analyses, the location of the crack tip was shown to be more accurate (*i.e.,* $\pm$ 120 μm) than classical (visual) procedures (of the order of $\pm$ 500 μm), which are operator-dependent since it is performed by analyzing pictures of the edge of the sample. The standard uncertainty in $\mathcal{G}$ values was shown to be at most equal to 50 J/m^2, which is significant but acceptable, for DCB tests for which a critical value of $\mathcal{G}$ is of the order of 400 J/m^2. Conversely, for the CLS test values as high as 1300 J/m^2 are determined, and even greater than 2000 J/m^2 at initiation. Thanks to the sub-pixel resolution of Q4-DIC, this new methodology, which is encapsulated in a unique tool, offers a safer and more robust evaluation compared with global and visual techniques.

The analysis of mode mixity shows that it can sometimes deviate quite significantly from the theoretical estimates based upon ideal loading conditions. The evaluation of the true boundary conditions was crucial to draw this type of conclusion. In particular, it is shown that passive (*i.e.,* lateral) confinements

have to be controlled in a very complex manner to ensure the quasi-pure mode II configuration for CLS configurations. One of the reasons being the Poisson contraction associated with the tensile load. For DCB experiments, when the two heights of the beams are not identical, small mode II contributions are observed. For all geometries and configurations, the mode mixity extracted at the local scale is more accurate than (former) global extractions since experimental boundary conditions are continuously accounted for during the propagation events.

5. Conclusions

In this paper, three tests were analyzed to determine critical propagation parameters in mode I and II conditions, and also a mixed mode I/II configuration by extension. This is achieved by coupling displacements fields measured by resorting to digital image correlation and finite element simulations. The common information is given by the measured displacements on the boundary of the region of interest that are the boundary conditions of the finite element simulations. By minimizing the distance between the measured and computed displacement fields, it is possible to determine the crack tip location. The latter being determined, energy release rates associated with each mode are evaluated by post-processing the finite element results. The *experimental* mode mixity is also accessible by following the procedure proposed herein for any of the analyzed geometries and configuration.

These encouraging results show that the identification of more advanced (cohesive) models of any interface parameters (*e.g.,* the stiffness of the interface) can be reached without any global sensor measurement, the two layers can be seen as a "stress gauge," provided their elastic properties are known and no intralaminar damage develops during the test. (Nonlinear contributions of the intralaminar behavior may also be accounted for in the present setting.)

Local kinematic fields may also be used to identify propagation parameters under more complex configurations (*e.g.,* interfaces between $[\pm\ \theta]$ plies) since the approach developed herein is very generic, and does not rest on closed-form solutions whose applicability is restricted to very simple cases. It also shows that it is possible to extract directly intrinsic propagation parameters (*e.g.,* $\mathcal{G}_{Ic}$ and $\mathcal{G}_{IIc}$), but also initiation values and a direct evaluation of the mode mixity even when it is not constant during the whole test. These emerging identification methods fully support the virtual testing approach in the way to reduce numerous classical tests with a poor quality of parameter extraction to the benefit of new identification methods with added value [41, 42, 43, 44]. They can also be used as a redundant check of any identification process or for local counter-expertise of any complex delamination process.

Acknowledgements

The support of this research by "Agence Nationale pour la Recherche" is gratefully acknowledged (VULCOMP Phase 1 project, grant number ANR-2006-MAPR-0022-01).

References

[1] Ladevèze P, Le Dantec E. Damage modelling of the elementary ply for laminated composites. Comp Sci Tech. 1992;43(3):257-67.

[2] Allix O, Blanchard L. Mesomodeling of delamination: towards industrial applications. Comp Sci Tech. 2006;66(6):731-44.

[3] ASTM D5528 - 01e3 Standard Test Method for Mode I Interlaminar Fracture Toughness of Unidirectional Fiber-Reinforced Polymer Matrix Composites. West Conshohocken, PA (USA): ASTM; 2007.

[4] ASTM D5868 - 01 Standard Test Method for Lap Shear Adhesion for Fiber Reinforced Plastic (FRP) Bonding. West Conshohocken, PA (USA): ASTM; 2008.

[5] Allix O, Corigliano A. Modeling and simulation of crack propagation in mixed-modes interlaminar fracture specimens. Int J Fract. 1996;77:111-40.

[6] Derewonko A, Godzimirski J, Kosiuczenko K, Niezgoda T, Kiczko A. Strength assessment of adhesive-bonded joints. Comput Mat Sci. 2008;43(1):157-64.

[7] Kanninen MF, Popelar CH. Advanced Fracture Mechanics. Oxford (UK): Oxford University Press; 1985.

[8] Pardoen T, Ferracin T, Landis CM, Delannay F. Constraint effects in adhesive joint fracture. J Mech Phys Solids. 2005;53:1951-83.

[9] Leffler K, Alfredsson KS, Stigh U. Shear behaviour of adhesive layers. Int J Solids Struct. 2007;44:530-45.

[10] Sørensen BF, Gamstedt EK, Østergaard RC, Goutianos S. Micromechanical model of cross-over fibre bridging - Prediction of mixed mode bridging laws. Mech Mat. 2008;40:220-34.

[11] Salomonsson K, Andersson T. Modeling and parameter calibration of an adhesive layer at the meso level. Mech Mat. 2008;40(1-2):48-65.

[12] Yang QD, Thouless MD, Ward SM. Elastic-plastic mode-II fracture of adhesive joints. Int J Solids Struct. 2001;38:3251-62.

[13] Su C, Wei YJ, Anand L. An elastic-plastic interface constitutive model: Application to adhesive joints. Int J Plasticity. 2004;20:2063-81.

[14] Sargent JP. Durability studies for aerospace applications using peel and wedge tests. Int J Adhesion Adhesives. 2005;25:247-56

[15] Abanto-Bueno J, Lambros J. Investigation of crack growth in functionally graded materials using digital image correlation. Eng Fract Mech. 2002;69:1695-711.

[16] Fedele R, Raka B, Hild F, Roux S. Identification of adhesive properties in GLARE assemblies by Digital Image Correlation. J Mech Phys Solids. 2009;57:1003-16.

[17] Ireman T, Thesken JC, Greenhalgh E, Sharp R, Gädke M, Maison S, et al. Damage propagation in composite structural elements-coupon experiments and analyses. Comp Struct. 1996;36:209-20.

[18] IGC 4.26.381. Instruction générale de contrôle pour la détermination du G1c. Aérospatiale standard (in French); 1991.

[19] AITM 1.0005. Determination of interlaminar fracture toughness energy. Airbus Industrie Test Method, Issue 2; 1994.

[20] Sutton MA, McNeill SR, Helm JD, Chao YJ. Advances in Two-Dimensional and Three-Dimensional Computer Vision. In: Rastogi PK, editor. Photomechanics. Berlin (Germany): Springer; 2000. p. 323-72.

[21] Sutton MA, Zhao W, McNeill SR, Helm JD, Piascik RS, Riddel WT. Local crack closure measurements: Development of a measurement system using computer vision and a far-field microscope. In: McClung RC, Newman Jr. JC, editors. Advances in fatigue crack closure measurement and analysis: second volume, STP 1343: ASTM; 1999. p. 145-56.

[22] Chasiotis I, Knauss WG. A New Microtensile Tester for the Study of MEMS Materials with the Aid of Atomic Force Microscopy. Exp Mech. 2002;42(1):51-7.

[23] Forquin P, Rota L, Charles Y, Hild F. A Method to Determine the Toughness Scatter of Brittle Materials. Int J Fract. 2004;125(1):171-87.

[24] Chasiotis (edt.) I. Special issue on nanoscale measurements in Mechanics. Exp Mech. 2007;47(1).

[25] Besnard G, Hild F, Roux S. "Finite-element" displacement fields analysis from digital images: Application to Portevin-Le Châtelier bands. Exp Mech. 2006;46:789-803.

[26] McNeill SR, Peters WH, Sutton MA. Estimation of stress intensity factor by digital image correlation. Eng Fract Mech. 1987;28(1):101-12.

[27] Geers MGD, De Borst R, Peijs T. Mixed numerical-experimental identification of non-local characteristics of random-fibre-reinforced composites. Comp Sci Tech. 1999;59:1569-78.

[28] Cho S, Cárdenas-García JF, Chasiotis I. Measurement of Nanodisplacements and Elastic Properties of MEMS via the Microscopic Hole Method. Sensors and Actuators A. 2005;120:163-71.

[29] Maier G, Bocciarelli M, Fedele R. Some innovative industrial prospects centered on inverse analyses. In: Mróz Z, Stavroulakis G, editors. Parameter

Identification of Materials and Structures CISM Lecture Notes: Springer Verlag, Wien; 2005. p. 47-73.

[30] Hild F, Roux S. Digital image correlation: From measurement to identification of elastic properties - A review. Strain. 2006;42:69-80.

[31] Abanto-Bueno J, Lambros J. Experimental Determination of Cohesive Failure Properties of a Photodegradable Copolymer. Exp Mech. 2005;45(2):144-52.

[32] Simulia. Abaqus Analysis User's Manual (version 6.7) 2010.

[33] http://www.holo3.com/correli-stc®-afr17.html

[34] Sih GC, Paris PC, Irwin GR. On cracks in rectilinearly anisotropic bodies. Int J Fract Mech. 1965;1:189-203.

[35] Simulia. Contour integral evaluation (section 11.4.2). Abaqus Analysis User's Manual (version 6.7) 2010. See also Stress intensity factor extraction (section 2.16.2). Abaqus Theory Manual (version 6.7) 2010.

[36] Rice JR. A Path Independent Integral and Approximate Analysis of Strain Concentrations by Notches and Cracks. ASME J Appl Mech. 1968;35:379-86.

[37] Parks DM. A stiffness derivative finite element technique for determination of crack tip stress intensity factors. Int J Fract. 1974;10(4):487-502.

[38] Russel AJ, Street KN. Moisture and temperature effects on the mixed-mode delamination fracture of unidirectional graphite epoxy. Delamination and debonding of materials: ASTM , Philadelphia (PA), USA; 1985. p. 349-70.

[39] Rhee KY. Characterization of delamination behavior of unidirectional graphite/PEEK laminates using cracked lap shear (CLS) specimens. Comp Struct. 1994;29:379-82.

[40] Lévêque D. Analyse de la tenue au délaminage des composites stratifiés : identification d'un modèle d'interface interlaminaire [PhD thesis]: ENS Cachan; 1998.

[41] Ben Azzouna M, Périé J-N, Guimard J-M, Hild F, Roux S. On the identification and validation of an anisotropic damage model by using full-field measurements. Int J Damage Mech. 2011;20(8):1130-50.

[42] Cox B, Yang Q. In Quest of Virtual Tests for Structural Composites. Science. 2006;314:1102-7.

[43] González C, LLorca J. Virtual fracture testing of composites: A computational micromechanics approach. Eng Fract Mech 2007;74:1126-38.

[44] Davies GOA, Ankersen J. Virtual testing of realistic aerospace composite structures. J Mat Sci 2008;42(20):6586-92.

List of Figures

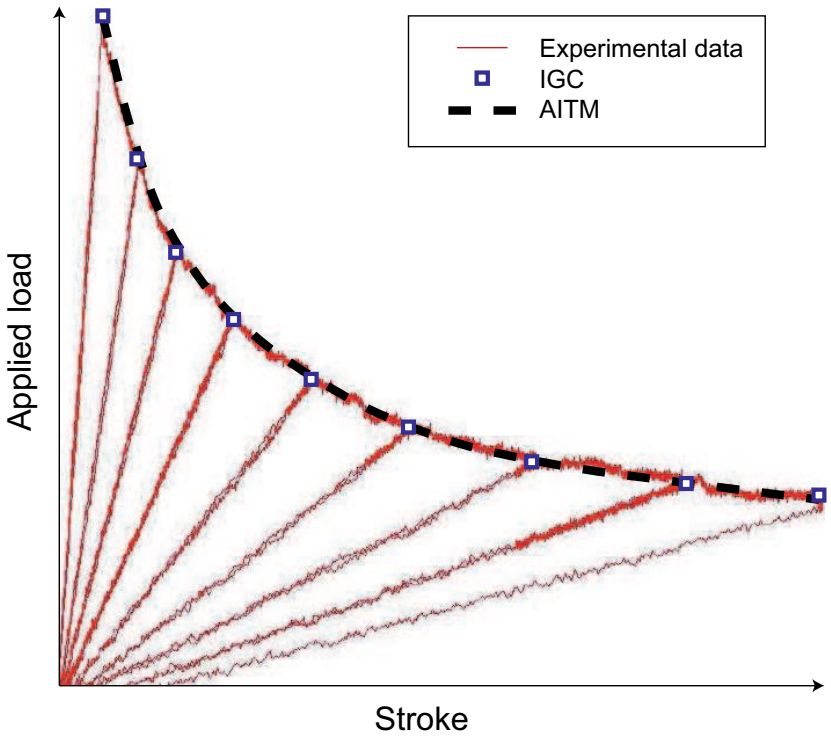

Figure 1: Different identification methods for the toughness of a DCB test from the applied load versus stroke curve. AITM method: one mean value is extracted from all the experimental data. IGC method: one value per cycle is determined. In the method developed herein each picture pair can be used to evaluate the current energy release rates and mode mixities

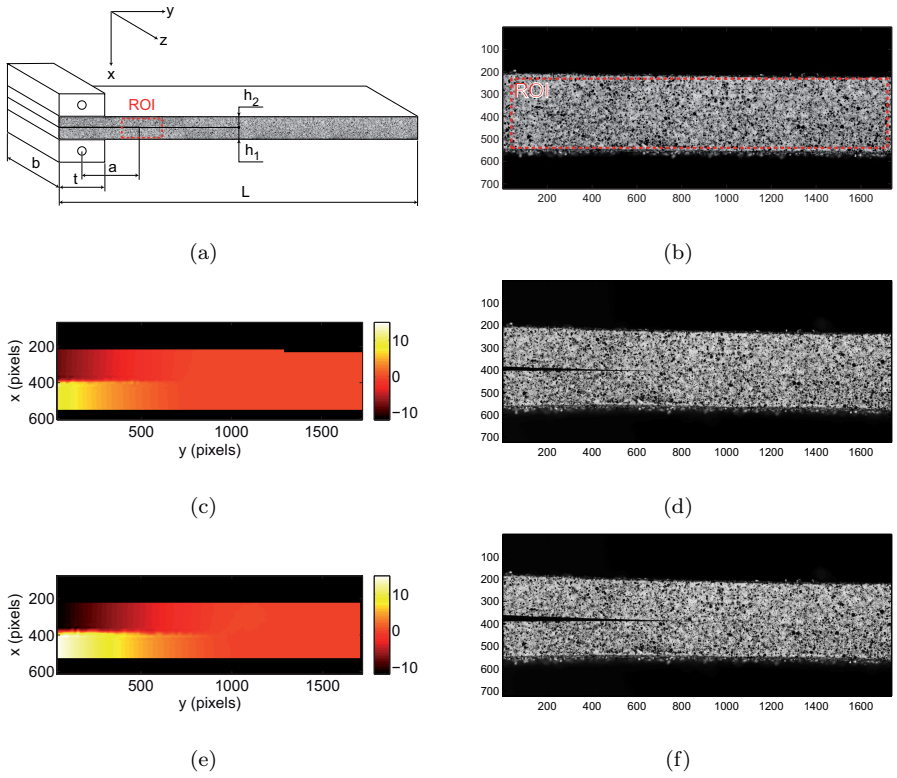

Figure 2: (a): DCB sample and location of the Region of Interest to analyze locally the displacement field in the vicinity of the crack tip. (b): Reference picture of the experiment. (c,e): Vertical displacement fields (in pixels) from which the rigid body motions have been subtracted (1 pixel $\leftrightarrow$ 12 μm). 16-pixel Q4 elements are used in the DIC analysis. (d,f): Corresponding pictures in the deformed configuration

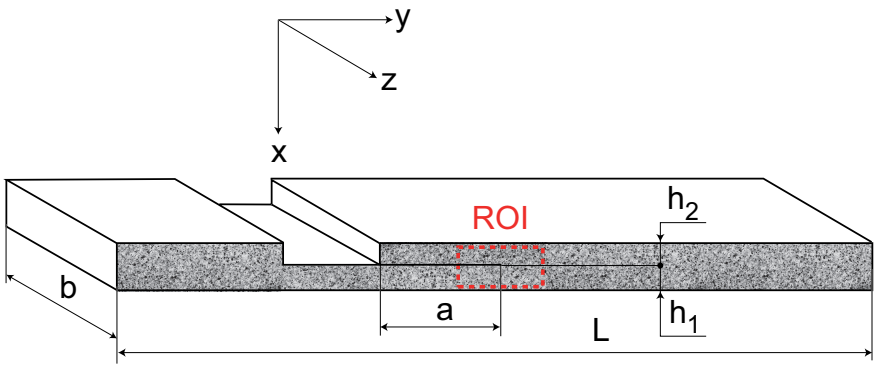

(a)

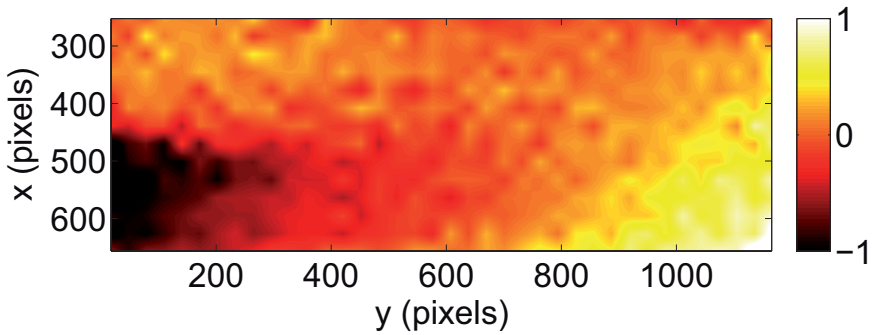

(b)

Figure 3: (a): CLS sample and location of the Region of Interest to analyze locally the displacement field in the vicinity of the crack tip. (b): Horizontal displacement field (in pixels) from which the rigid body motions have been subtracted (1 pixel $\leftrightarrow$ 6 μm). 32-pixel Q4 elements are used in the DIC analysis

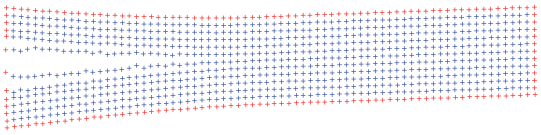

(a) Deformed mesh determined by Q4-DIC. The measured displacements of nodes in red are prescribed in FE analyses. The inner nodes (in blue) are used to minimize the identification error δ

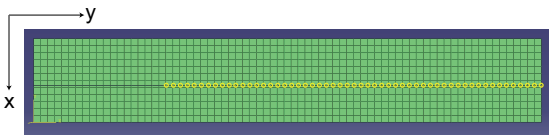

(b) FE mesh in which the interface nodes that are not broken are marked in yellow

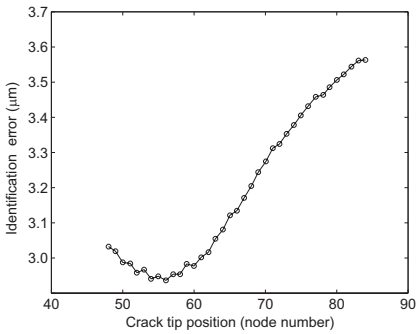

(c) Change of the identification error δ as a function of the assumed position for the crack tip

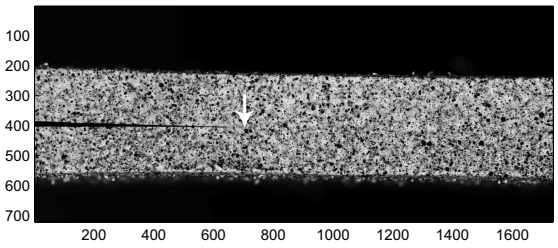

(d) Optimal crack tip position marked with white arrow

Figure 4: Different steps for the determination of the crack tip position

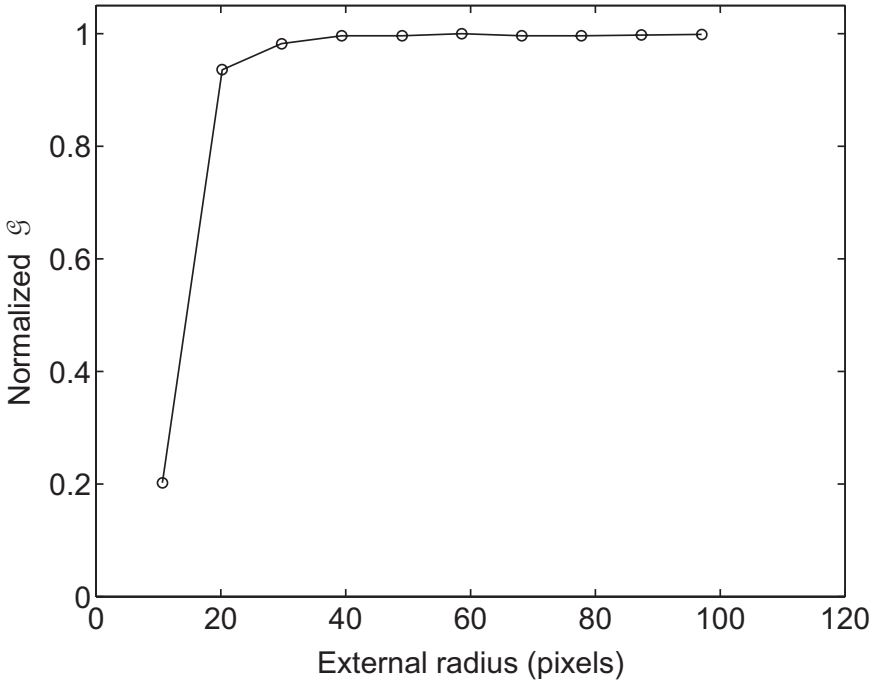

Figure 5: J-integral normalized by its maximum value as a function of the external radius of the integration domain. For an external radius greater than 32 pixels, the evaluation of $J = \mathcal{G}$ is independent of its value

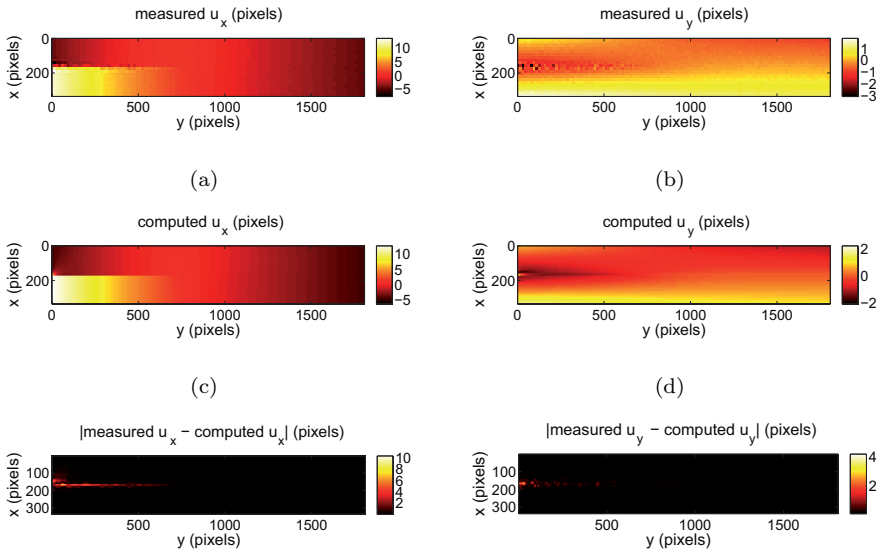

Figure 6: (a,b): Measured, (c,d): computed, and (e,f): residual displacement fields in the vertical (left) and horizontal (right) directions (1 pixel $\leftrightarrow$ 12 μm) for the DCB experiment

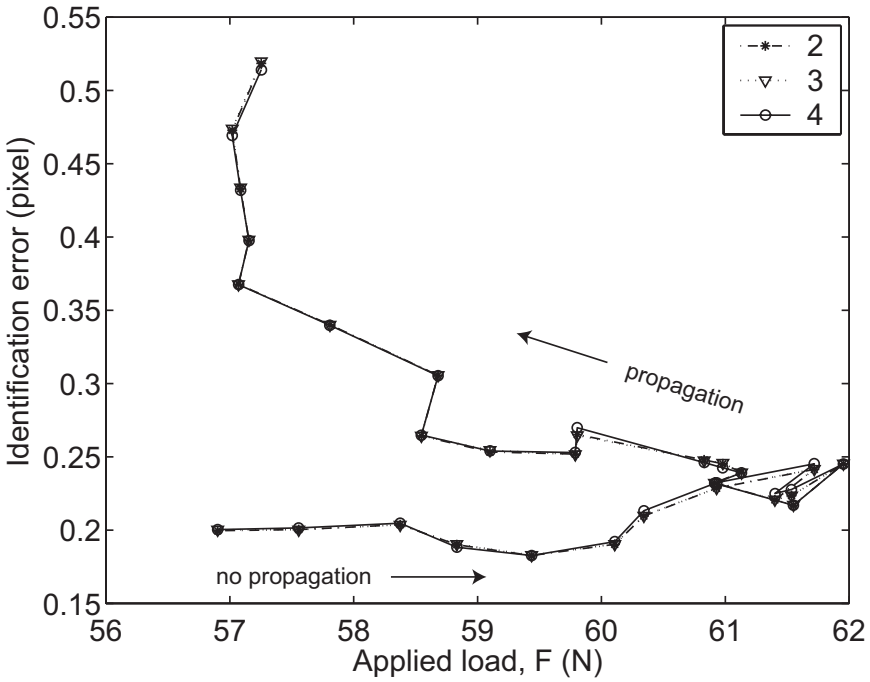

Figure 7: Change of the identification error δ with the refinement index ρ for the 28 load levels of the DCB experiment (1 pixel $\leftrightarrow$ 12 μm). The first part corresponds to a load increase with no propagation, and the second part is associated with a load decrease during crack propagation

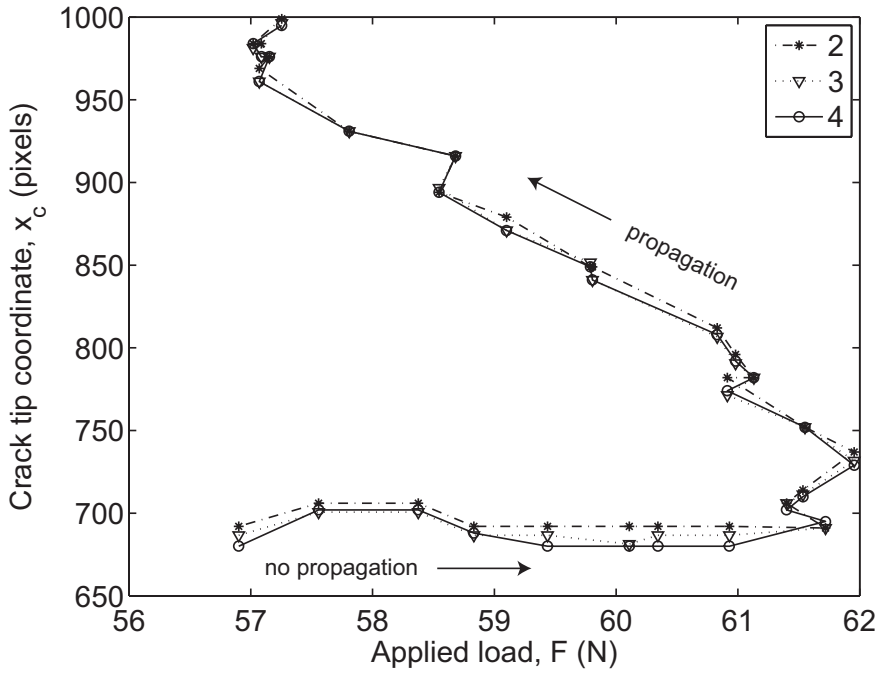

Figure 8: Crack tip position as a function of the applied load level for three different refinement indices ρ for the DCB experiment (1 pixel $\leftrightarrow$ 12 μm). The first part corresponds to a load increase with no propagation, and the second part is associated with a load decrease during crack propagation

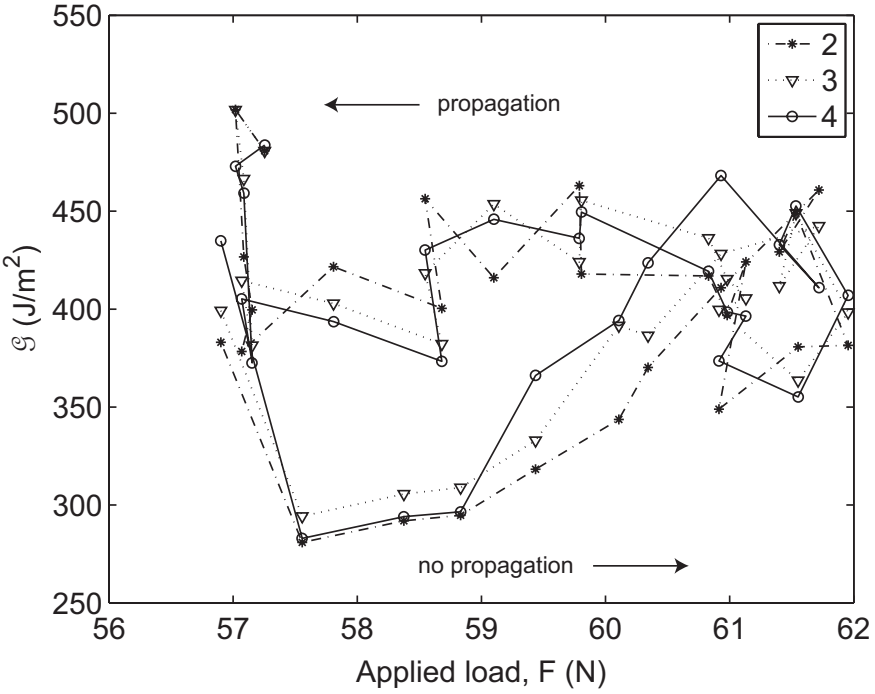

Figure 9: $\mathcal{G}$ as a function of the applied load level for the three refinement indices ρ for the DCB experiment. The first part corresponds to a load increase with no propagation, and the second part is associated with a load decrease during crack propagation

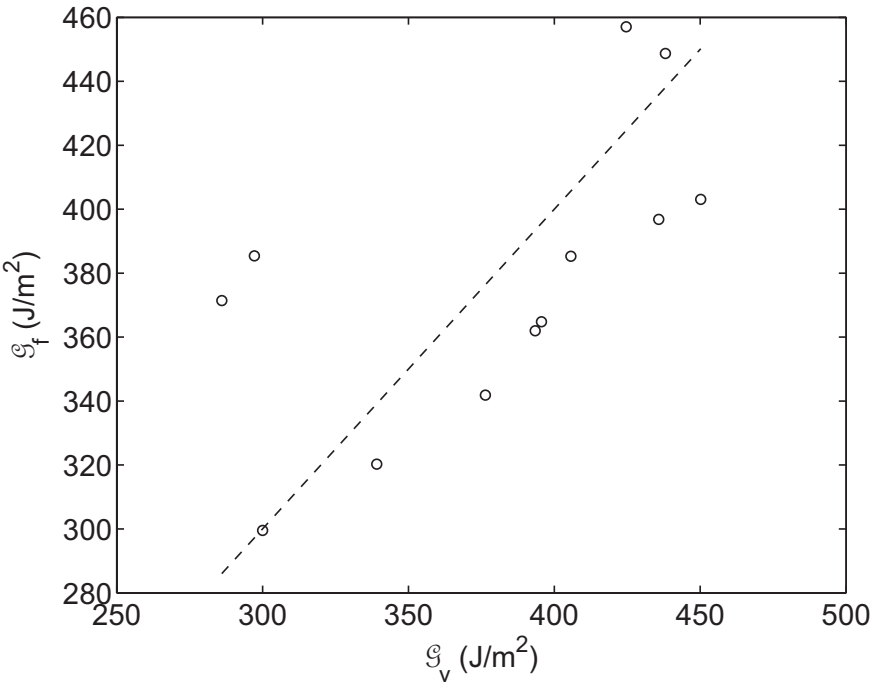

Figure 10: Sensitivity of $\mathcal{G}$ with respect to the crack tip position. Comparison of $\mathcal{G}$ determined for a fixed crack tip position ($\mathcal{G}_f$) as a function $\mathcal{G}$ determined for a variable crack tip position ($\mathcal{G}_v$, see Figure 9) for the DCB experiment. The dashed line corresponds to a linear interpolation of slope equal to 1. The RMS difference between the two estimates is of the order of 50 J/m^2

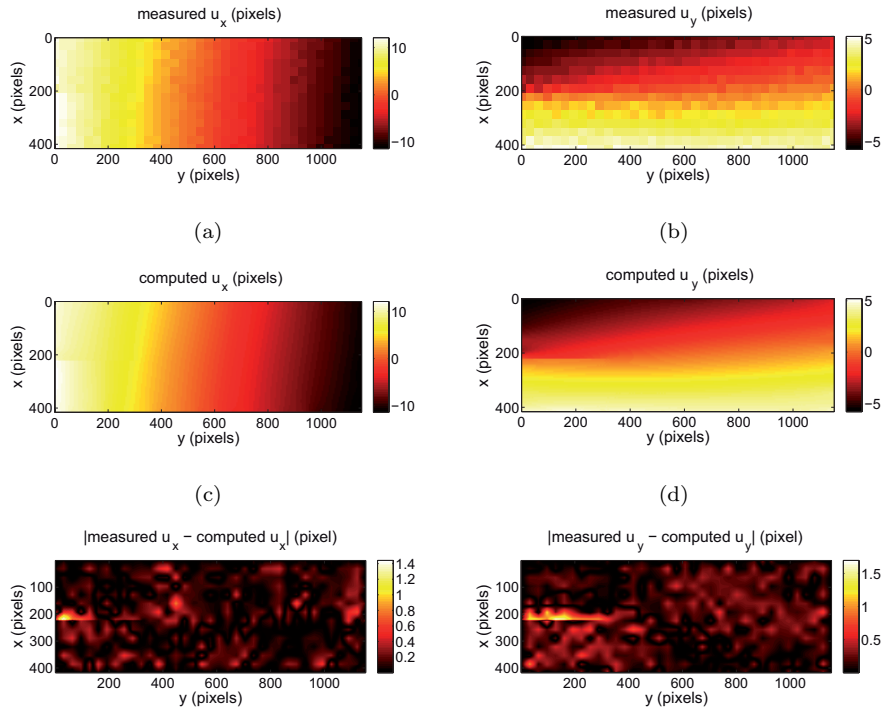

Figure 11: (a,b): Measured, (c,d): computed and (e,f): residual displacement fields in the horizontal (left) and vertical (right) directions for the 9 kN load level of the modified CLS experiment (1 pixel $\leftrightarrow$ 6 μm)

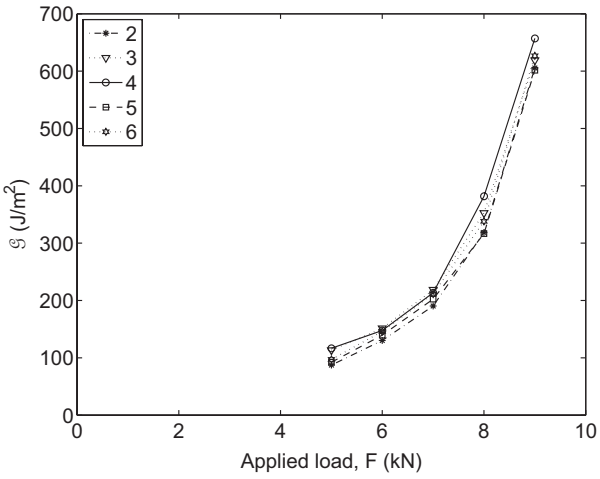

(a)

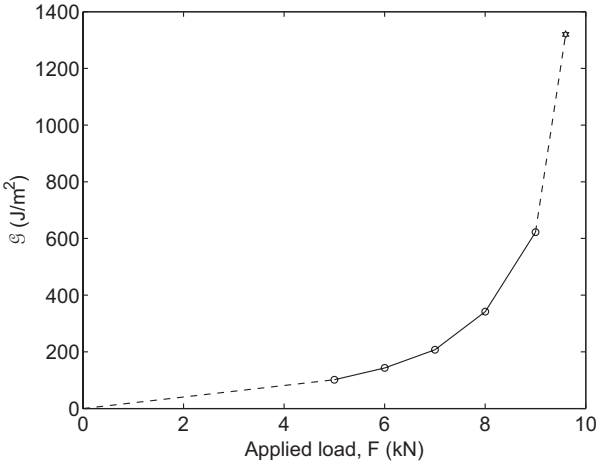

(b)

Figure 12: -a-Change of $\mathcal{G}$ with the refinement index ρ for the five load levels (CLS experiment). A 16 J/m^2 RMS difference is observed when the different results are compared. -b-Average $\mathcal{G}$ as a function of the applied load. The hexagram corresponds to the evaluation of the critical value by using Equation (1)

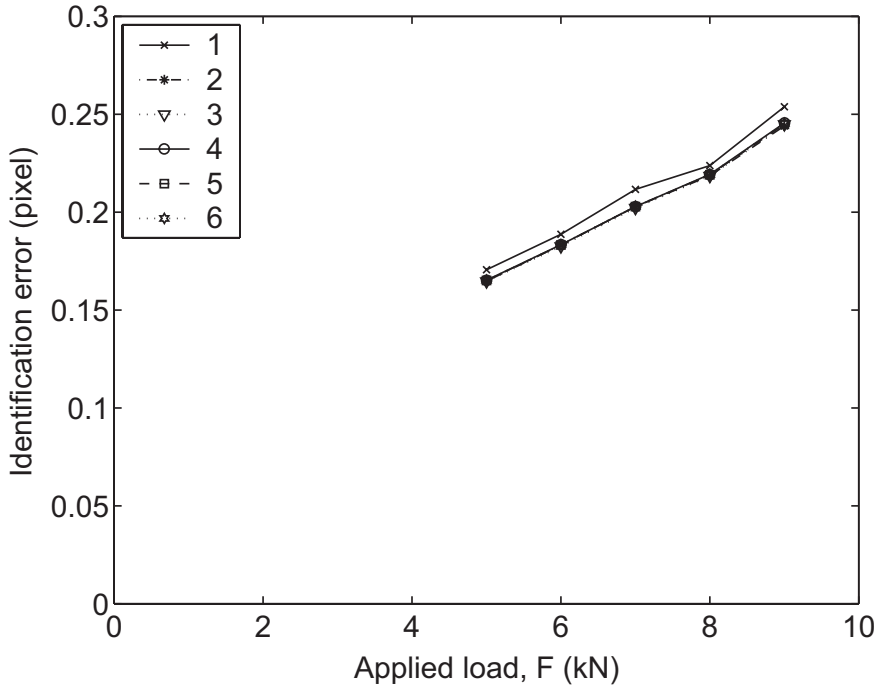

Figure 13: Change of the identification error with the refinement index ρ for the five load levels of the modified CLS experiment (1 pixel $\leftrightarrow$ 6 μm)

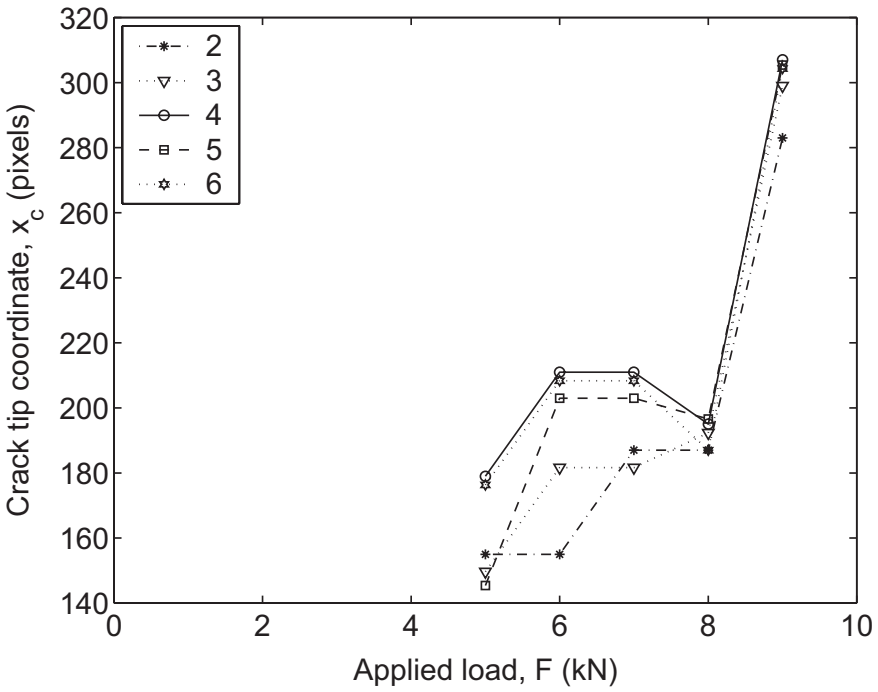

Figure 14: Crack tip position as a function of the applied load level for five refinement indices ρ for the modified CLS experiment (1 pixel $\leftrightarrow$ 6 μm)

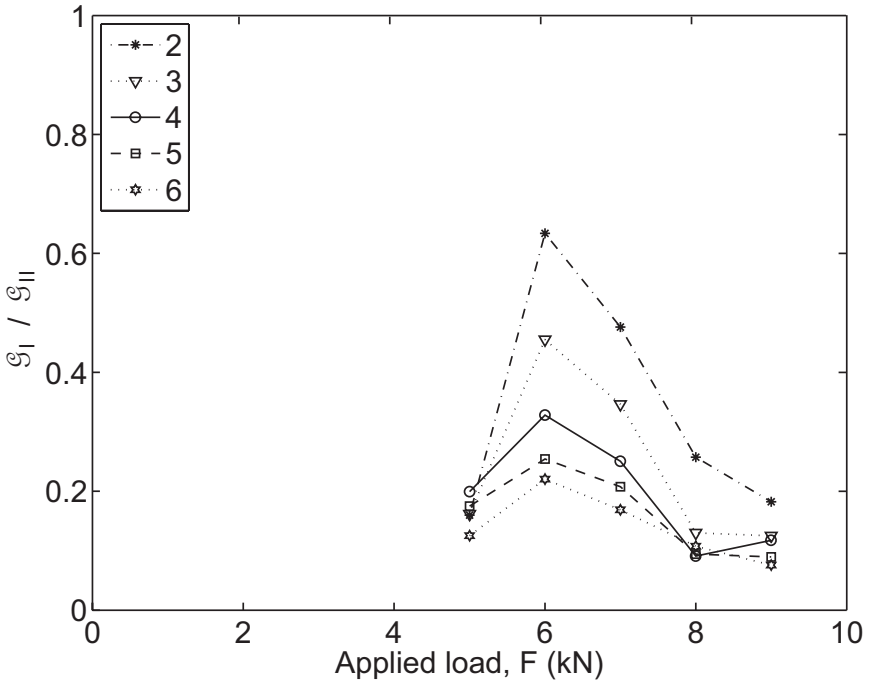

Figure 15: Energy release rate ratio as a function of the applied load level for the modified CLS experiment

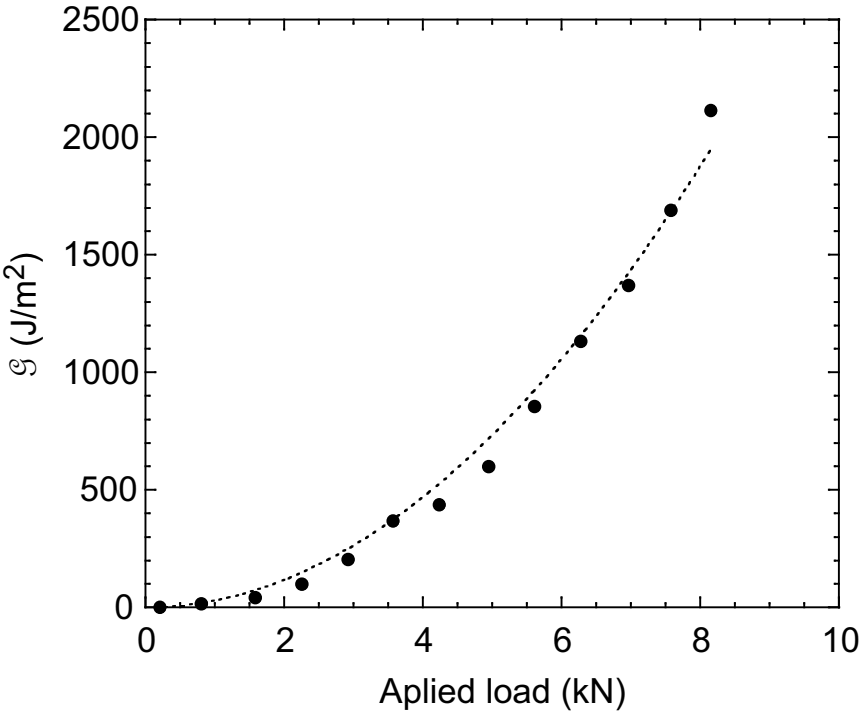

Figure 16: $\mathcal{G}$ as a function of the applied load level for the initiation step of the CLS experiment. The dashed line corresponds to a parabolic interpolation

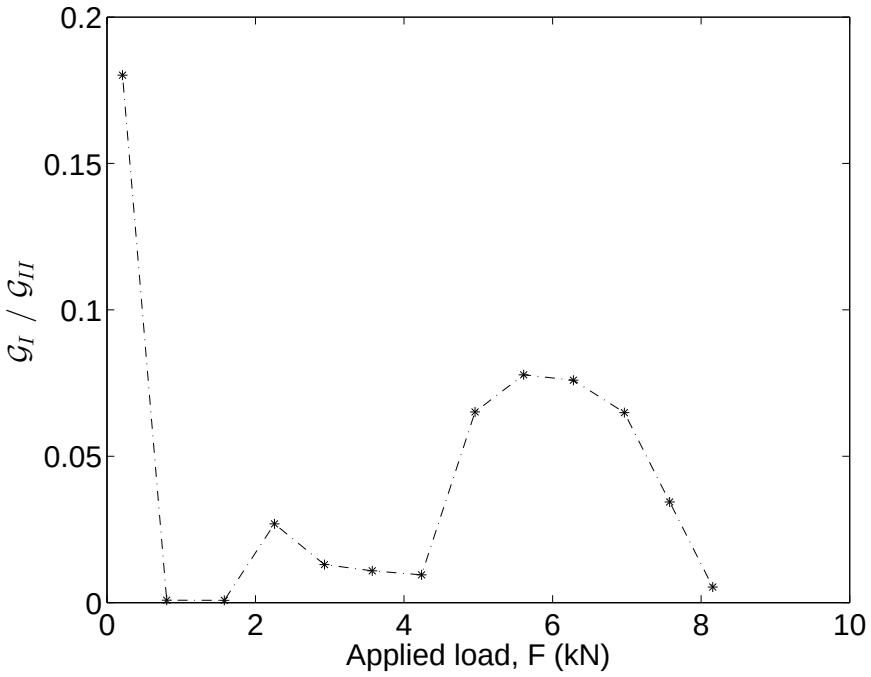

Figure 17: $\mathcal{G}_I/\mathcal{G}_{II}$ ratio as a function of the applied load level for the initiation step of the CLS experiment

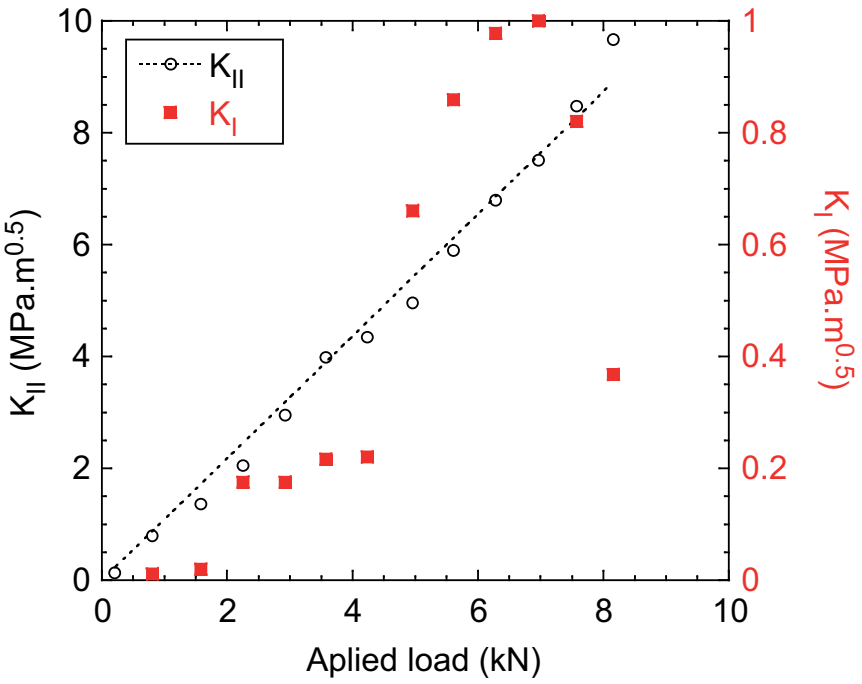

Figure 18: Mode I and II SIFs as functions of the applied load level for the initiation step of the CLS experiment. The dashed line corresponds to a linear interpolation

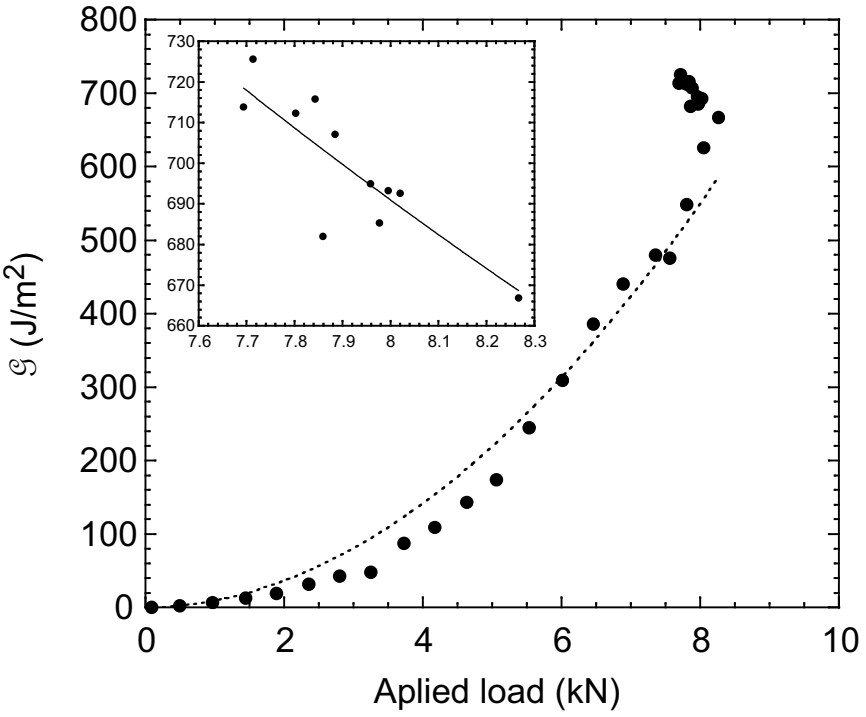

Figure 19: $\mathcal{G}$ as a function of the applied load level for the propagation step of the CLS experiment. The dashed line corresponds to a parabolic interpolation. Inset: detail of the propagation history. The solid line corresponds to a hyperbolic interpolation

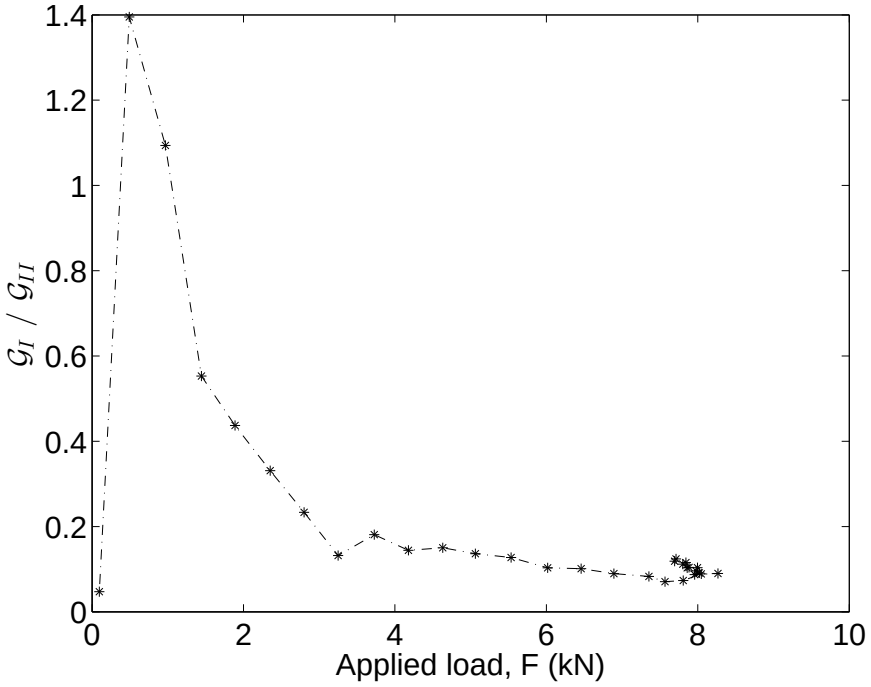

Figure 20: $\mathcal{G}_I/\mathcal{G}_{II}$ ratio as a function of the applied load level for the propagation step of the CLS experiment